Physica Medica 137 (2025) 105068

Contents lists available at ScienceDirect

Physica Medica

journal homepage: www.elsevier.com/locate/ejmp

Original paper

Bragg peak position monitoring using silicon and titanium nanoparticles as prompt-gamma tracers

Bartosz Klębowski [a,*,1], Barbara Kołodziej [b,c,d,*,1], Barbara Beus [e], Magdalena Garbacz [a], Ronja Hetzel [e], Jonas Kasper [e], Aleksandra Kaszlikowska [b], Andrzej Magiera [b], Aleksandra Wrońska [b]

[a] Institute of Nuclear Physics Polish Academy of Sciences, 31-342 Kraków, Poland
[b] Marian Smoluchowski Institute of Physics, Jagiellonian University, 30-348 Kraków, Poland
[c] Department of Adult Neurology, Medical University of Gdansk, 80-210 Gdańsk, Poland
[d] The Translational Brain Disease Centre of the Fahrenheit Union of Universities, Medical University of Gdańsk, 80-210 Gdańsk, Poland
[e] III. Physikalisches Institut B, RWTH Aachen University, Aachen, Germany

ARTICLE INFO

Keywords:
Tracers
Simulations
Nanoparticles
Proton Therapy

ABSTRACT

Purpose: Spherical silicon and rods-like titanium oxide nanoparticles (NPs) have been analyzed for use in the proton range verification method in proton therapy (main goal), as well as radiosensitizers (second goal) in this therapy due to their physical and biological properties. The method involved the use of tracers emitting prompt-gamma radiation during irradiation with protons. The basic assumption of the method is to selectively deliver the tracer in form of NPs to the tumor. The cytotoxicity of the obtained nanomaterials was also checked against normal and cancer cells.

Methods and Materials: Correlation between the Bragg peak (BP) position in the PMMA phantom and the signal emitted by the analyzed tracers were determined on the basis of simulations carried out using the Geant4 toolkit. To determine the cytotoxicity of nanosilicone and nanotitanium, as well as their radiosensitizing properties a classic MTS test and a modified multiple MTS test were performed. The location of both types of NPs was determined using holotomographic microscopy.

Results: For silicon NPs, a signal was observed when the BP was located entirely in the structure imitating a tumor and decreased when the BP was entirely outside the structure. In the case of titanium NPs, the signal did not correlate with the position of the structure mimicking a tumor. Both types of NPs at low concentrations turned out to be non-toxic to both cell lines. It has been shown that both types of nanoparticles have promising radiosensitizing properties, in particular towards cancer cells.

Conclusions: When it comes to physical properties, silicon appears to be an optimal candidate for use in proton therapy monitoring. Moreover, the silica NPs turned out to be slightly more effective radiosensitizers than titanium NPs.

1. Introduction

Proton therapy is one of the most modern and precise cancer treatments available. However, its efficacy can still be improved by reducing the safety margins, i.e. the tumor envelope of healthy tissue included in the target region in proton therapy, to mitigate the uncertainty of proton range determination. Today, many methods, including those based on prompt gamma radiation (PG), are being developed to allow in situ and in vivo verification of the beam range, thus progressing in therapy [1]. These methods verify the range of protons and the conformity of the administered dose with the previously established treatment plan. In reality, beside the tumor displacement resulting from the finite accuracy of patient positioning, both the tumor shape and volume may change in the course of the therapy, and so may the tumor surrounding, due to the weight variation of the patient. Although there are strategies under development to mitigate those effects, known as adaptive proton

* Corresponding authors.
E-mail addresses: bartosz.klebowski@ifj.edu.pl (B. Klębowski), barbara.kolodziej@gumed.edu.pl (B. Kołodziej).
[1] These are two equal first authors.

https://doi.org/10.1016/j.ejmp.2025.105068
Received 21 December 2024; Received in revised form 13 July 2025; Accepted 7 August 2025
Available online 11 August 2025

therapy, they have not become standard in clinical practice yet [2].

Some efforts have been made to include patient movements and anatomical changes that may occur in the course of therapy (such as weight reduction) into treatment plans [3]. Nowadays, 4-D treatment planning methods are developed to take into account respiratory movements during irradiation of lung tumors [4,5].

However, both uncertainties related to the determination of the range of the proton beam and those arising from the variable position of the tumor could be reduced by employing a method that allows the registration of signals originating specifically from components present only in cancerous tissue.

The idea of using tracers, selectively delivered to the tumor and activated with a proton beam, has been presented in [6]. These tracers, whose nuclei undergo excitation in interactions with beam protons, emit their characteristic gamma radiation only during irradiation. This radiation, when detected, can serve to tag the situation that the proton beam indeed irradiates the tumor and not the neighboring tissues, allowing the reduction of the routinely applied safety margins. The concept has been further explored from the biological side in [7] and from the technical side in [8], where the detection feasibility and statistical significance of the PG tracer signal were experimentally investigated. The use of non-radioactive elements to increase the statistics of registered PG was also described in [9] or to provide information about when the maximum of the energy deposit moves out of the target volume, as in the case of endorectal balloon idea presented in [10].

The most appealing aspect of the beam-activated tracer method is the fact that the detection setup does not rely on careful positioning with respect to the patient. Also, no assumptions about the details of the tumor geometry are needed. Assuming that the tracer is accumulated only in the tumor, the tracer PG signal appears only when the tumor tissues are irradiated. In this sense, the method has a built-in coordinate frame related to the tumor, it is self-orienting.

The authors of [11] proposed using tracers in the form of nanoparticles (NPs), which are another hot topic in tumor research.

By definition, NPs are objects having a diameter between 1 and 100 nm [12]. These NPs are characterized, among others, by stability, the possibility of their biofunctionalization, high surface-to-volume ratio and – sometimes – magnetic properties [13]. Due to these features, they are also more and more often used in biomedicine. One of the applications of these NPs is to improve the effectiveness of radiation-based anticancer therapies. Such NPs, called radiosensitizers, make cells more sensitive to subsequent irradiation. Importantly, radiosensitizers in low concentration do not cause a decrease in cell survival by themselves, and only a combined effect with irradiation is observed. In particular, high-Z metal NPs have found wide applications as radiosensitizers, e.g. gold, platinum, silver and oxides: zinc, bismuth, hafnium, titanium and iron [13–26]. As a result of the interaction of radiation (photon or proton) with high-Z metal NPs, a significant amount of reactive oxygen species (ROS) is generated, which can interact with the DNA of cells causing its double-stranded, irreversible damage and finally – cell death [27]. Thus, NPs-assisted irradiation would allow to reduce the total radiation dose and decrease the side effects of such therapy. There are also other mechanisms of radiosensitization using NPs, such as inhibition of the cell cycle in the G2/M (radiation-sensitive) phase, the so-called bystander effect or lipid peroxidation [28,29]. In the context of the potential use of NPs in medicine, it is important to consider a range of their properties, such as appropriate biodistribution, biodegradability, and the possibility of surface functionalization. For example, the smallest NPs, i.e., those smaller than 5 nm, are efficiently filtered by the kidneys and excreted in the urine. In turn, NPs with a larger nm size exhibit increased stability in the bloodstream and are less prone to rapid clearance. They often accumulate in organs such as the liver, spleen, and kidney [30,31]. A major issue with the biomedical use of 'raw' metallic NPs is their low biodegradability. On the other hand, an advantage of such metallic NPs is the ease of their functionalization due to the active surfaces of the metal cores. This enables straightforward formation of bonds between the NPs and various functional groups, most commonly thiol groups (–SH). Therefore, proper functionalization of such nanoparticles using biodegradable ligands may facilitate their subsequent degradation and reduce accumulation in the body [32,33].

Our work presents the investigation of selected tracer candidates: titanium and silicon in the form of nanoparticles (the primary objective of the study). The studies are performed using both Monte Carlo simulations and experiments. From the physical side, the dependence of the PG signal strength on the tracer concentration, and the spatial correlation of the signal strength with the location of the Bragg peak inside the tumor are determined using Monte Carlo simulations. Biological aspects are addressed in a series of *in-vitro* tests with cell cultures. In addition to assessing the potential use of these NPs as tracers, preliminary studies were also conducted on their radiosensitizing potential in simulated proton therapy (a secondary objective of the study).

2. Materials and methods

2.1. Selection of tracer candidates

Tracer candidates must meet certain criteria to be used in practice. Those criteria were divided into two categories: physical and biological.

The following physical properties are demanded from tracer candidates:

1. They should emit gamma quanta only after irradiation by a proton beam, i.e. be stable elements.
2. The energy of the emitted gamma quanta should be unique and different from those of other elements common in human tissues. An energy range of 0.7–3 MeV is preferred to ensure good detector resolution and efficiency and low background, but the limits are not rigid.
3. The lifetime of the excited state should not exceed 1 μs.
4. The maximum cross section to produce the tracer response should be for the low-energy protons, which ensures the correlation between the Bragg peak position in the tumor and the appearance of the tracer signal.

As for the biological aspects, they are as follows:

1. The element has to be delivered to the tumor only.
2. The necessary concentration of the tracer cannot be toxic to healthy tissues during delivery to tumor cells and after irradiation.
3. The form used to deliver the element to the tumor should maintain its stability from injection through to the completion of irradiation, as well as stability for storage.
4. Efficiency of the synthesis method.
5. The element should be accessible in the injection mode.
6. Ideally, the delivery form of the element should increase the radiosensitivity of tumor cells, thereby enhancing the effectiveness of proton therapy.

Among the potential tracer candidates, initially the following elements have been considered: silicon, calcium, chromium, iron, titanium and magnesium.

TALYS 1.95 program [34] was used to calculate the cross sections of gamma emission which occurs after excitation by a proton beam for each of those isotopes. In this investigation, only gammas originating from deexcitation from the first excited level were considered, as those gammas are expected to dominate for the lowest proton energies. The cross sections are depicted in Fig. 1, along with the proton energy deposition and range in water, obtained using the SRIM-2013 program [35].

Furthermore, we checked the neighborhood of the spectral lines listed in Fig. 1 in the experimental PG spectra obtained in our previous

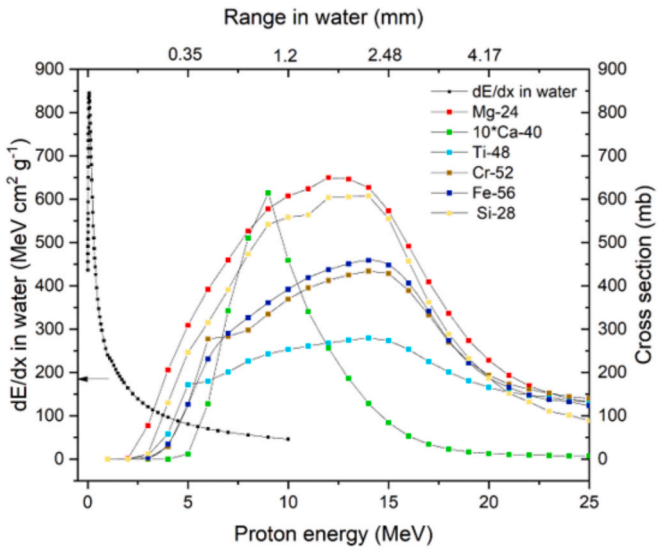

Element	E_1 [MeV]	Element	E_1 [MeV]
Mg-24	1.37	Ca-40	3.35
Ti-48	0.98	Cr-52	1.43
Fe-56	0.85	Si-28	1.78

Fig. 1. Cross section of proton-induced gamma emission from the first excited state for various elements versus the energy of protons, calculated using TALYS 1.95 [30]. The top axis shows the residual range of protons with a certain energy in water, obtained from SRIM-2013 [31]. The black points and the curve show the proton energy deposits [31] with the respective axis on the left. Below the figure, energies of gamma quanta emitted at the deexcitation from the first excited states are listed.

studies with a PMMA phantom and a proton beam [1,36].

There, the signal peaks should be sufficiently far from other PMMA peaks to form a distinct signal.

Finally, we decided to begin our experimental studies on tracers from silicon and titanium, as we had NPs containing those two elements available. These materials also seemed to be a good starting point for other reasons. Silicon has been demonstrated to be useful in PG spectroscopy aiding prostate cancer treatment [10], although the method proposed there was different from ours. Silicon-based NPs are additionally characterized by high biocompatibility and easy of functionalization Titanium, on the other hand, is a commonly used biocompatible material for intracorporeal implants, such as markers, prosthetics, and reinforcing screws [37]. Although the synthesis of titanium oxide NPs usually requires the use of organic solvents (which may potentially increase their cytotoxicity), titanium oxide NPs are known to induce ROS in cells, enhancing the radiosensitizing effect. Further in the article, certain biological aspects will be investigated, such as whether the maximum non-toxic concentration of nanoparticles containing silicon or titanium is sufficient to observe a statistically significant tracer signal, and whether the presence of these nanoparticles increases the radiosensitivity of selected cancer cells. Other biological criteria will be the subject of further studies planned within the group.

2.2. Synthesis of nanoparticles and their characterization

2.2.1. Synthesis of titanium nanorods (Ti NRs)

All reagents for the NPs synthesis were purchased from Sigma Aldrich. Ti NRs were synthesized according to [38] with minor changes. Briefly, 1.6 ml oleic acid and 6 ml 1-octadecene were mixed in the 50 ml three-neck flask. The reaction mixture was degassed at 80 °C with argon for 1 h. Then, 0.3 ml of titanium isopropoxide was injected and the mixture was heated for 20 min. A color change of the solution from colorless to yellow was observed, indicating titanium oleate complex formation. The release of isopropyl alcohol – a by-product of the reaction – was observed. The reaction mixture was heated to 260 celsius, and subsequently 0.32 ml oleylamine was added after 10 min of heating, which enabled the high-temperatured aminolysis of titanium oleate and the growth of monodisperse anatase Ti NRs. The reaction continued for 1 h and then the solution was cooled to room temperature. The obtained NPs solution was purified by centrifugation several times in hexane (20 min,15000 rpm) and then in increasingly polar solvents (acetone, ethanol and water).

2.2.2. Synthesis of Fe3O4- SiO2 core–shell nanoparticles (FeSi NPs)

FeSi NPs were obtained according to the recipe from [39] without any modification.

2.2.3. Scanning transmission electron microscopy

Scanning transmission electron microscopy (STEM) with a high-angle annular dark-field detector (HAADF) was used to evaluate the morphology of the synthesized Ti NRs and FeSi NPs. The measurements were made on an aberration-corrected FEI Titan electron microscope (Hillsboro, OR, USA) operating at 300 kV equipped with a FEG (field emission gun) cathode. The size distribution of the NPs was assessed on the basis of the STEM photographs (from different areas of the STEM grids). For Ti NRs, both short and long-axis lengths were estimated. For FeSi NPs the size of the core (Fe_3O_4) and the shell (SiO_2) were determined.

2.3. Biological tests in vitro

2.3.1. Cell culture

Two cell lines were used for the experiment: glioblastoma multiforme cells (U-118 from the American Type Culture Collection) and normal human lung fibroblasts (NHLF from Lonza Bioscience) as control. The U-118 cells were cultured in DMEM (Dulbecco's modified eagle medium) containing 4 mM L-glutamine, 4500 mg/L glucose, 1 mM sodium pyruvate and 1500 mg/L sodium bicarbonate (ATCC, Manassas, VA, USA). The NHLF cells were cultured in FGM™-2 (Fibroblast Growth Medium-2 BulletKit™, Lonza Bioscience, Basel, Switzerland). Both media were supplemented with 10 % fetal bovine serum (FBS) and 1 % mixture of antibiotics (penicillin, streptomycin and neomycin). The cells were cultured by bi-weekly passages at 37 °C in a humidified atmosphere with 5 % CO_2.

2.3.2. Proton beam irradiation protocol

Proton irradiation was performed in the Cyclotron Centre Bronowice, Institute of Nuclear Physics Polish Academy of sciences using the IBA Proteus C-235 isochronous cyclotron (Louvain-la-Neuve, Belgium) with a compact conventional magnet and two gantries equipped with a scanning nozzle. Proton irradiation was carried out at room temperature using a monoenergetic field (field size 20 cm x 20 cm). Radiation dose of 2 Gy was used, as the standard dose in glioblastoma multiforme radiotherapy is a total dose of 60 Gy divided into 30 fractions (2 Gy for each fraction) [40].

2.3.3. MTS viability assay and multiple MTS radioresistance test

A classic MTS (3-(4,5,-dimethylthiazol-2-yl)-5-(3–carboxymethoxyphenyl)-2-(4–sulfophenyl)–2H-tetrazolium) survival test (CellTiter 96® Aqueous One Solution Cell Proliferation Assay, Promega, Madison, WI, USA) was used to evaluate the cytotoxicity for the obtained NPs. The cells were cultured in flat-bottom 96-well plates at a density of 10^4 cells per well in the appropriate medium. After 48 h of culture, 20 μl of NPs (aqueous solution) were added to 100∼μl medium giving the final mass concentration of NPs in medium from 0.01 to 2 %. After 24 h of incubation, 20 μl of MTS dye solution was added per well. The amount of produced formazan, which is proportional to the number of viable cells, was determined by measuring the absorbance ($\lambda = 490 \sim$ nm) with a 96-well plate reader (Multiskan SkyHigh Plate Reader,

Thermofisher, Waltham, MA, USA). The cell viability can be estimated by measuring the ratio of the absorbance of cells cultured with NPs to the absorbance of the control (cells without NPs). Experiments were done in triplicate. For further studies of irradiation effects on cells with a proton beam, the concentration of 1 % for both U118 and NHLF cells were used. After irradiating the cells with a proton beam, a modified MTS test (multiple MTS assay) was performed to evaluate the effectiveness of such simulated therapy [41]. Multiple MTS assay was performed once every day. Similar to the classical MTS assay, after various incubation times of the cells (1-4 days) with NPs/proton beam, 20 μl of MTS was added, and after 2 h of incubation, the absorbance was measured.

2.4. Holotomographic microscopy

Holotomographic microscopy enables real-time and nanoscale observation of interaction between cells and NPs. Using this method, a three-dimensional refractive index (RI) distribution matrix is obtained. Thanks to differences in RI, it was possible to image the cell membrane, cytoplasm and NPs in cells. Holotomographic imaging was carried out using the holotomographic 3D Cell Explorer-Fluo (Tolochenaz, Switzerland) microscope. The cells were placed in a 96-well plate (special for fluorescence imaging) at the density of $8 \bullet 10^3$ per well in the DMEM medium without phenol red. After 24 h, Ti NRs or FeSi NPs were added to each well, obtaining a final concentration of 1 %. Holotomographic images were taken before the addition of NPs, as well as 24 h after incubation of NPs with cells. Then, 3D holotomographic images were reconstructed based on the RI index using the STEVE Software, enabling the assessment of the NPs localization in cells.

2.5. Geant4 simulations

Prompt-gamma signals from the selected elements were investigated using Monte Carlo simulations in the Geant4 toolkit [42], version 6.10. This software is widely used in research related to proton therapy, for example in range uncertainty studies [3] or treatment plan verification [43]. According to the studies presented in [34], the most suitable physics models in research on proton therapy are provided by the QGSP_BIC_HP_EMZ physics list and this one was used in simulations. Further details can be found in [44] and Guide for Physics Lists, Geant4 Collaboration, 2017 [45].

2.6. Tracer signal significance

To determine the minimum tracer concentration, which provides a statistically significant signal, we performed simulations of a box phantom made of PMMA doped with a tracer. The PMMA phantoms are widely used in prompt gamma radiation studies [46]. Unlike water, in addition to hydrogen and oxygen, it also contains carbon, also present in human tissues. This allows us to obtain more complete information about the expected neighborhood of the analyzed peaks forming the signal. Several mass concentrations (0,5%, 1 %, 1,5%, 2 %) of tracers were examined. The dimensions of the box were 6 x 6 x 30 cm^3. The proton beam energy was set to 180 MeV and the number of shot protons was $2.3 \cdot 10^6$ in each of those simulations. All produced gamma quanta were registered independent of their direction of emission. This corresponds to a situation in which a detector of the geometrical acceptance of A = 0.0077 registers gamma quanta produced by $3 \cdot 10^8$ protons, i.e., an upper limit of the number of protons per spot in a typical treatment plan [47]. The detector acceptance was obtained assuming the use of a spectroscopy detector similar to the one used in [42] with the radius of 3.5 cm, the distance between the detector front surface and the beam axis of 20 cm.

2.7. Depth profile of the tracer signal

To determine the spatial correlation between the tracer signal and the position of the Bragg peak, simulations were performed with a different geometry and modified Geant4 settings. It was noticed that in the QGSP_BIC_HP_EMZ model the Doppler broadening was overestimated [48].

In our simulations, the Lorentz boost was turned off, which allowed us to obtain spectra with a more realistic energy resolution, comparable with that observed in [36].

The irradiated phantom was a 15 x 13.5 x 13.5 cm^3 cuboid made of PMMA. The dimensions have been selected so that they are close to the average dimensions of a human head. The elemental composition of PMMA ensures that the prompt gamma radiation emitted after irradiation by a proton beam will be comparable to that emitted by the human body. The central 5 x 5 x 5 cm^3 part of the phantom has been enriched with tracer elements in 1 % or 2 % mass fraction. Two types of nanoparticles were used: silicon and titanium, of the properties described in Section *Synthesis of nanoparticles*. Additional elements forming the NPs have been included in appropriate proportions. However, the geometric distribution of the elements (i.e., the NP form) has not been taken into account. This insert mimicked a tumor located in the central part of the head.

The phantom was irradiated by 81 parallel proton beams, distributed evenly on a square plane perpendicular to the direction of the protons, to achieve the maximum dose in the tracer-enriched part of the phantom. The single beam source was a circle with a radius of 2.5 mm and the distance between neighboring sources was 5 mm.

The vertex coordinates as well as the momentum vectors of the gammas originating in the phantom were recorded. Neutrons originating from the phantom were not propagated in the simulations to reduce the computational cost. Firstly, neutrons do not form discrete structures in the energy spectrum, but a continuum. Secondly, their abundance at the detection angle of 90° is about four times lower than that of the gammas in the Ti and Si signal regions. The results of initial simulations justifying this approach are presented in Fig. 1 in the Supplementary Material. A commercially available high-purity germanium detector was assumed for gamma detection. Assuming the detector radius of 2 cm and its distance from the beam axis of 19 cm, the acceptance of the setup was A = 0.0027 of the full solid angle. The number of protons was determined on the basis of parameters from the Cyclotron Centre Bronowice. According to [49], the number of protons needed to administer the dose of 2 Gy is about 10^8 per spot. The exact number depends on proton energy, but in simulations we neglected this dependence to simplify the implementation. Moreover, to accelerate the simulations, the population of simulated beam protons impinging on the target was reduced by detector acceptance similarly as in Section *Tracer signal significance*, resulting in 271,605 protons per beam, and all the produced gammas were registered and taken into account for analysis.

Energies of protons were selected to probe the tracer signal profile along the phantom at several depths, in particular close to the boundaries of the insert. The following set of beam energies was simulated: 85, 88, 92, 95, 100, 110, 118, 123, 128, 132 and 136 MeV. The selection of the beam energies was motivated by the depth profiles of the deposited dose, that are presented in the Results section. A schematic of the irradiated setup, beam geometry, and Bragg peak positions for the simulated beam energies are shown in Fig. 2.

As a result of the deexcitation of silicon and titanium nuclei from the first excited state to the ground state, gamma quanta are emitted with energies of 1.78 MeV and 0.98 MeV, respectively. The analysis of the energy spectra obtained from Geant4 simulations was performed using the ROOT framework [50].

For both tracers, silicon and titanium, the number of signal gamma quanta N_γ was calculated as the difference between the spectrum integral in the peak region N and the background. The background contribution N_B was approximated by fitting a quadratic function with

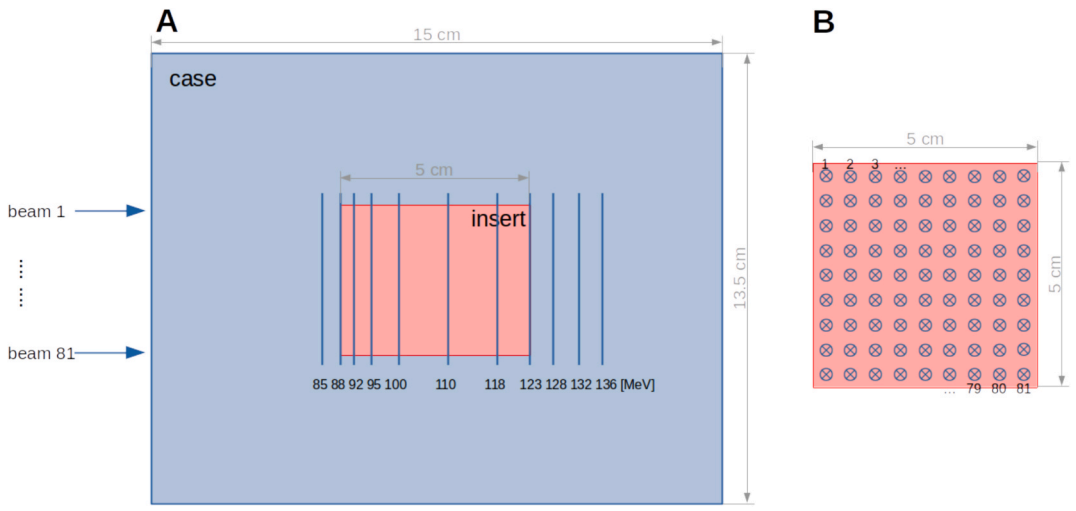

Fig. 2. A simulation scheme including the phantom geometry with the tracer-doped part. A) side view; vertical lines indicate the depths corresponding to the positions of Bragg peaks for individual simulated beam energies. B) front view of the insert (zoomed in).

parameters p_0, p_1, p_2. The final formula was the following:

$$N\gamma = N - \frac{1}{w}\int_l^u (p_0 + p_1\mathbf{E} + p_2\mathbf{E}^2)d\mathbf{E}, \quad (1)$$

where u and l denote the upper and lower end of the signal region, and w represents the histogram bin width.

The uncertainty of the integral representing the background contribution was calculated using the following formula:

$$(\sigma(N_B))^2 = \mathbf{t}^T\mathbf{X}\mathbf{t}, \quad (2)$$

where **X** represents the covariance matrix and **t** is defined as

$$\mathbf{t} = \left[\frac{\partial N_B}{\partial p_0}, \frac{\partial N_B}{\partial p_2}, \frac{\partial N_B}{\partial p_2}\right]. \quad (3)$$

Thus, the final uncertainty of the signal N_γ was calculated as follows:

$$\sigma(N_\gamma) = \sqrt{\left(\sqrt{N}\right)^2 + (\sigma(N_B))^2} \quad (4)$$

3. Results

3.1. STEM analysis

The morphology (size and shape) of both fabricated NPs types were evaluated by electron microscopy. STEM images of Ti NRs and FeSi NPs with the corresponding size distributions are depicted in Fig. 3.

Fig. 3A1, shows that the obtained TiO_2 NPs look like nanorods with an average length of 25 nm and 3 nm for the long and short axes, respectively (Fig. 3A2) and are not agglomerated. The nanorods make

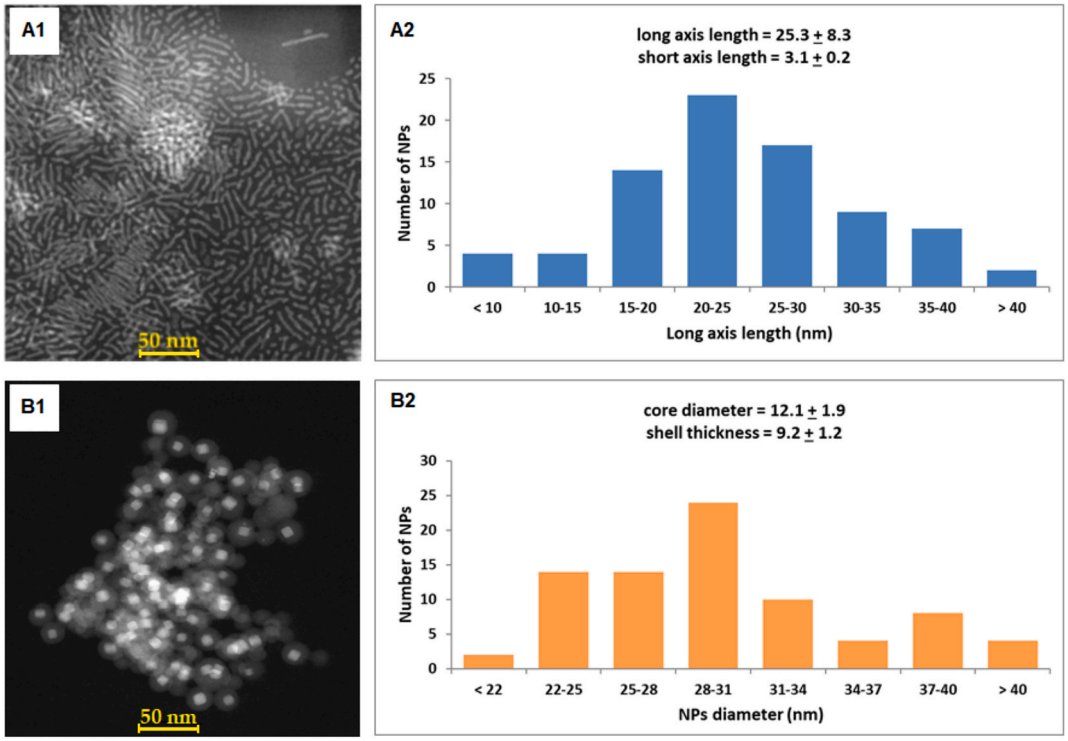

Fig. 3. HAADF STEM images of A1) Ti NRs and B1) FeSi NPs with the corresponding size distributions (A2 and B2, respectively).

up the majority of all NPs, however, single spherical TiO_2 NRs are also visible. Fig. 3B1 shows the morphology of the FeSi NPs, showing Fe_3O_4 core SiO_2-shell NPs. The cube-shaped Fe_3O_4 core has an average diameter of 12 nm (Fig. 3B2) and is clearly distinguishable, because it has a strong contrast due to its higher Z number ($Z_{Fe} = 26$) compared to Si ($Z_{Si} = 14$). The Fe_3O_4 cores are surrounded by a continuous ~ 9 nm SiO_2 shell. It is worth noting that most of the NPs visible on the STEM photograph have a core–shell structure, however single NPs consisting of SiO_2 alone are also visible.

3.2. Determination of NPs cytotoxicity – MTS assay

The viability of cells cultured with TiO_2 NRs and FeSi NPs was determined using the MTS test. Therefore, the cytotoxicity of NPs with a wide spectrum of mass concentration against two cell lines was investigated. The results are depicted in Fig. 4.

The trend was that both cell lines showed a decrease in survival with increasing concentration of TiO_2 NRs and FeSi NPs, respectively. Based on the MTS test results, it was established that for the normal NHLF cells, the maximum non-toxic concentration (not causing a decrease in survival by more than 25 %) is 1.5 %, while for U-118 tumor cells – 1.0 %. Lower sensitivity of normal cells to NPs was expected and is consistent with numerous publications [51–54]. In general, there are no significant differences in the cytotoxic effect of both tested NPs.

For further in vivo tests, allowing to study the effect of the proton beam on cells cultured with NPs, the mass concentration of 1 % was chosen for both NHLF and U-118 lines, in order to be able to reliably compare the effect of such combined therapy on both types of cells.

3.3. Efficiency of combined proton irradiation of cells using nanoparticles – Multiple MTS assay

The multiple colorimetric MTS assay was used to evaluate proliferation and determine the survival fraction (SF) of cells cultured with NPs and exposed to a proton beam. The absorbance is directly proportional to the number of cells (at test in the phase of exponential growth), which was also consistent with the cell counts performed using Burker chamber. This fact was used to determine the SF according to the below formula:

$$SF = 2^{\frac{-t_{delay}}{t_{doubling}}} \quad (5)$$

where t_{delay} is the delayed time – the time period to reach a specific absorption value of control vs irradiated cells, $t_{doubling}$ is the time it takes for the cell population to double [35,55].

Based on the above formula, as well as the cell growth curves (see Fig. 2 in the Supplementary Material), SF was determined for control cells and cells irradiated with the proton beam in the presence of the NPs. The determined SF values are listed in Table 1.

Based on the above results, it is found that the radiation dose = 2 Gy caused only a slight decrease in SF for both tested cell lines. In turn, a combined effect is seen for proton irradiation in the presence of TiO_2 NRs and FeSi NPs. This effect is stronger for the U-118 glioblastoma multiforme cells. For these cells, there is also a significant difference in the radiosensitizing effect of these NPs in favor of FeSi NPs.

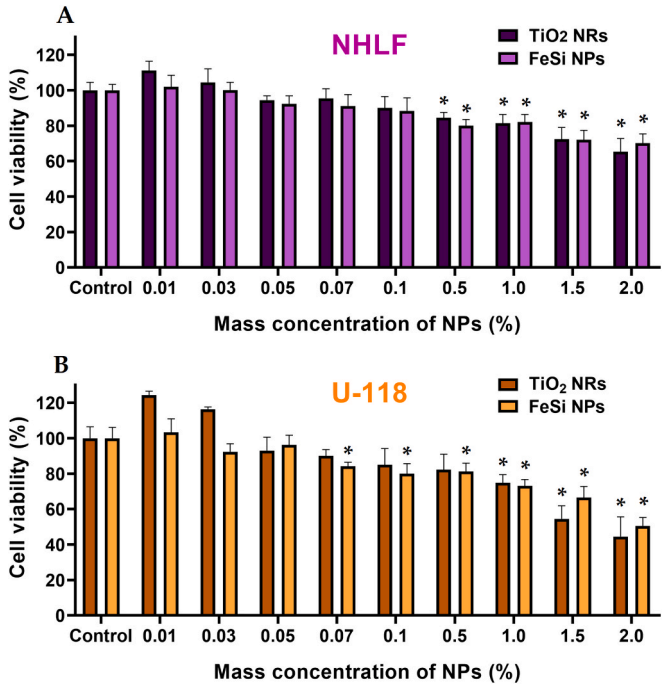

Fig. 4. Cytotoxicity of TiO_2 NRs and FeSi NPs against A) NHLF and B) U-118 cells after 24 h of incubation. The above data were analyzed by one-way analysis of variance (ANOVA) followed by the post hoc Tukey test. Differences were considered significant when p-value < 0.05 vs control. Test results are shown as the means ± standard error of the mean. Each experiment was performed in triplicate.

3.4. Holotomography imaging – Localization of NPs

To evaluate the interaction (in real time) between the cells and the NPs, the holotomographic imaging was performed. This technique provides information about the distribution of the 3D refractive index distribution within the cells. Moreover, information about the volume occupied by NPs in cells was also obtained. The results for the NHLF cells are depicted in Fig. 5, while for the U118 glioblastoma cells – in Fig. 6.

Holotomographic images of NHLF cells (Fig. 5 A) showed that after 24 h of cells incubation with both types of tested NPs, no visible cell damage or reduction in their number in the field of view was observed. Moreover, a larger flattening of these cells was observed, which means that – despite the presence of these NPs – they are able to grow properly and divide. A similar effect was observed for U118 cells (Fig. 6 A), although there was no such intense cell growth here. In the case of a toxic effect of these NPs, a change in their shape to spherical one would be observed (due to a decrease in their ability to adhere to the bottom of the plate), or even the fragmentation of these cells into small elements. These results confirm that the selected concentration of 1 % is not harmful to the tested cells. Based on Fig. 5 A and 6 A, as well as 5B and 6B (being a reconstruction of the Z-axis), the place of NPs accumulation in cells was determined. In order to better illustrate the procedure for determining the location of NPs in cells, sample films were prepared (see Supplementary Material, Movie 1 and Movie 2). For the NHLF cells, both FeSi and TiO_2 NRs tend to localize on the outer and inner parts of the cell membrane. In turn, in glioma U118 cells, NPs are distributed irregularly inside the cells and do not have one preferred location. Furthermore, using STEVE Software, distribution of refractive index with the value of refractive index volume corresponding to the NPs, cytoplasm and cell membrane was determined (see Supplementary Material, Fig. 3). The results are summarized in Table 2.

For normal NHLF cells (which is consistent with Fig. 5), cell growth and division were noticed over time, which is observable in the form of

Table 1
Multiple MTS assay results – survival fraction (SF) of control and irradiated cells cultured with(out) NPs. Test results are shown as the means ± standard error of the mean. Each experiment was performed in triplicate.

	NHLF	U-118
Control	100.0 % ± 5.2 %	100.0 % ± 3.7 %
Protons	89.3 % ± 2.4 %	82.4 % ± 3.1 %
Protons + TiO_2 NRs	71.2 % ± 4.0 %	58.3 % ± 2.1 %
Protons + FeSi NPs	73.1 % ± 3.6 %	51.0 % ± 2.4 %

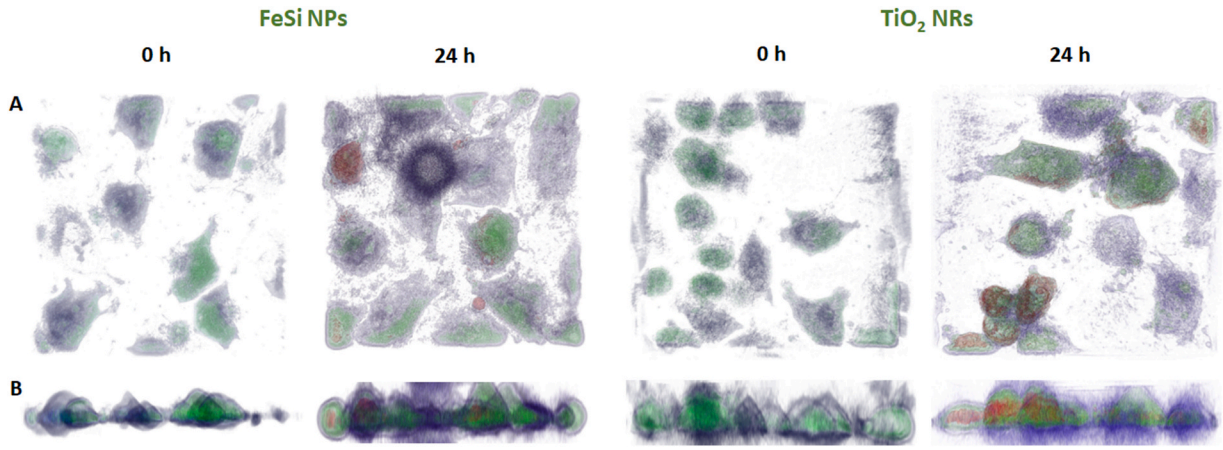

Fig. 5. A) 3D holotomographic images of NHLF cells before addition of NPs and cells cultured with FeSi NPs and TiO_2 NRs after 24 h of incubation reconstructed based on the refractive index of NPs (red color), cytoplasms (green color) and cell membrane (blue color). B) Z-axis reconstruction of holotomographic images. (For interpretation of the references to color in this figure legend, the reader is referred to the web version of this article.)

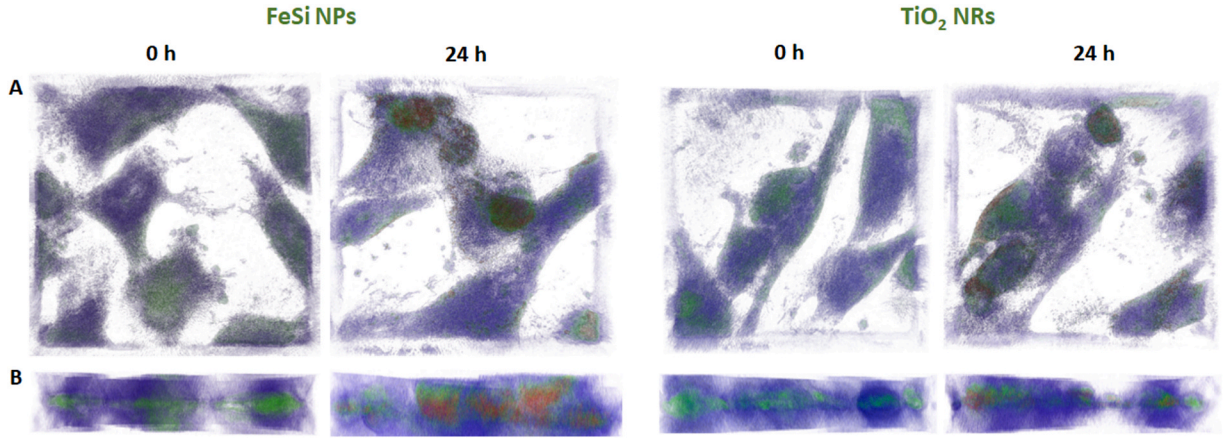

Fig. 6. Same as in Fig. 5 for U118 cells.

Table 2
Values of refractive index volume (μm^3) corresponding to the NPs, cytoplasm and cell membrane for NHLF cells (top table) and U118 cells (bottom table).

	FeSi NPs		TiO2 NPs	
	Before adding NPs	**After 24 h incubation**	**Before adding NPs**	**After 24 h incubation**
NPs	–	1 572 ± 145	–	1 910 ± 134
Cytoplasm	6 212 ± 341	10 832 ± 975	9 698 ± 875	11 896 ± 972
Cell membrane	22 396 ± 1 112	57 209 ± 7 544	45 160 ± 4 843	62 514 ± 8 663
	FeSi NPs		**TiO2 NPs**	
	Before adding NPs	**After 24h incubation**	**Before adding NPs**	**After 24h incubation**
NPs	–	3 697 ± 244	–	2 238 ± 199
Cytoplasm	18 356 ± 1 384	13 228 ± 1 165	13 888 ± 1 245	13 480 ± 1 041
Cell membrane	106 862 ± 7 587	93 340 ± 4 144	146 557 ± 9 348	106 590 ± 12 511

an increase in the volume of the cell membrane and cytoplasm (Table 2 – top). The situation is different for glioma U118 cells (Table 2 – bottom). After 24 h there is a certain reduction in the volume of the cytoplasm and cellular membrane, indicating inhibition of cell growth. The increased uptake of FeSi NPs by glioma cells explains the strengthened radiosensitizing effect of these NPs compared to TiO_2 NRs (Table 2).

4. Bragg peak position versus signal from tracer

The silicon signal is conveniently located in the PG spectrum far from other peaks, while for titanium it overlaps to some extent with other spectral structures (see Fig. 4 in the Supplementary Material).

Fig. 7 presents the depth profiles of the deposited dose and the tracer signal. The latter profiles have been constructed based on the Monte Carlo truth information about the mother particle, gamma energy and its emission vertex, thus are not affected by experimental resolution. One can see that for the beam energies for which the Bragg peak is located close to the distal surface of the insert, the peak is already rather broad along the beam direction due to the energy straggling. Thus, energies differing by 5 MeV in that region were selected for simulations (123 and 128 MeV), corresponding to a beam range difference of 7 mm in PMMA, although the treatment plan would suggest rather a 3-MeV step.

The dependence between the beam energy and the signal from silicon and titanium is presented in Fig. 8. The signal is the number of

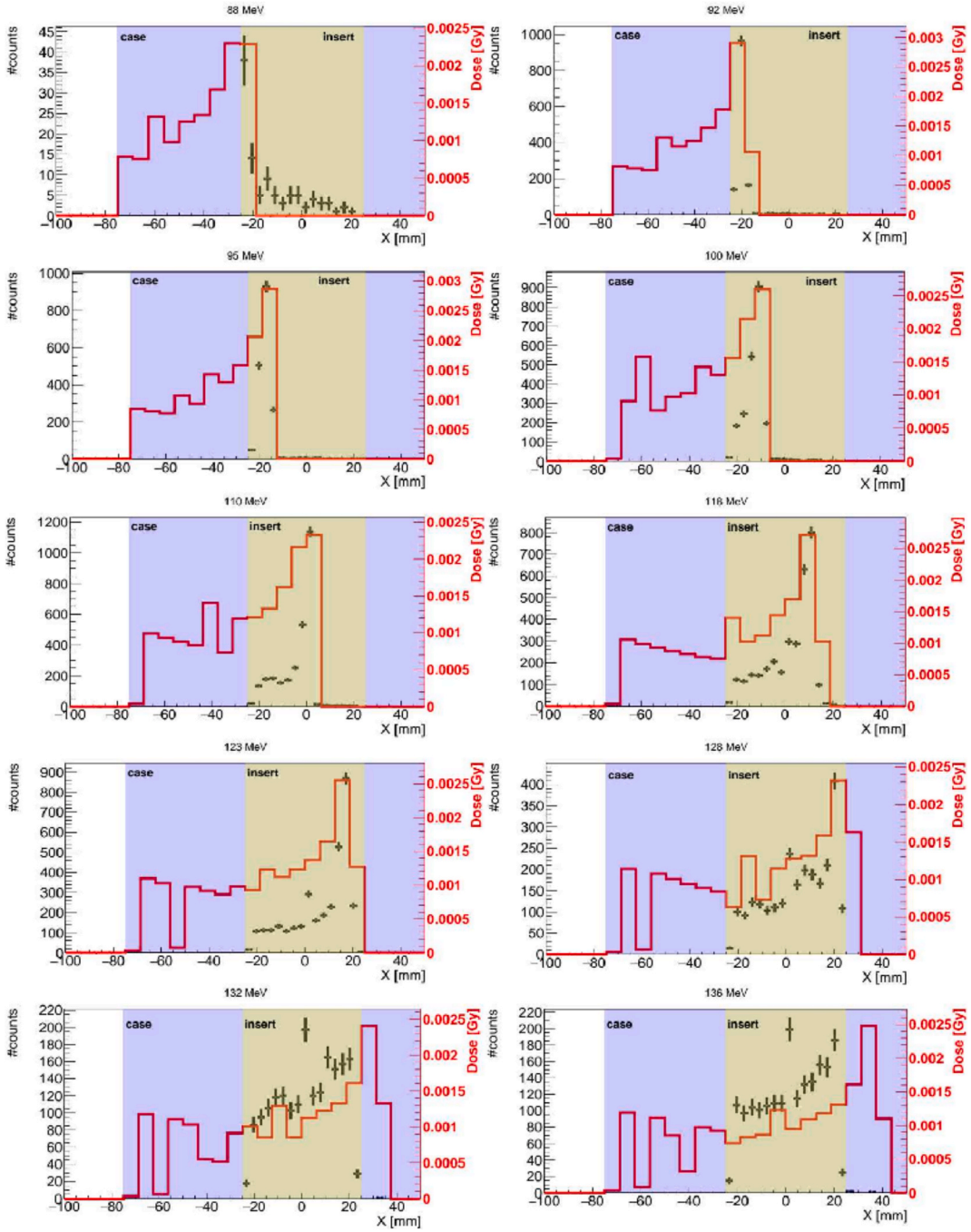

Fig. 7. Simulated depth profiles of deposited dose (red line) calculated for the number of protons reduced by assumed acceptance of the detector. The explanation of the approach can be found in Section Depth profile of the tracer signal. Overlaid is the depth profile of the silicon tracer signal (black points) obtained based on the Monte Carlo truth information (gamma quanta with energies 1.76–1.91 MeV and silicon as a mother particle). (For interpretation of the references to color in this figure legend, the reader is referred to the web version of this article.)

gamma quanta calculated using Formula (1). The uncertainties were obtained using Formula (4). The red parts of the panels represent the range of beam energies for which the Bragg peak is contained inside the insert.

5. Discussion

5.1. Nanoparticles investigation

The designed and synthesized nanoparticles based on titanium and silicon – despite differences in size, shape, as well as in the reagents used in the synthesis process – turned out to have similar cytotoxic and radiosensitizing properties, whereby U118 glioma cells were more sensitive to their actions. Both types of nanoparticles were characterized by a small size (well below 100 nm), which makes the surface-to-volume ratio of such nanomaterials very high. This increases the surface interaction of proton radiation with nanoparticles, consequently generating an increased amount of reactive oxygen species (ROS) causing significant cell damage. It should be emphasized that in the case of bimetallic FeSi nanoparticles, the final effect of biological tests could be influenced by both the interaction of cells with the iron core and the generally biocompatible silicon shell. Nanoparticles probably change the

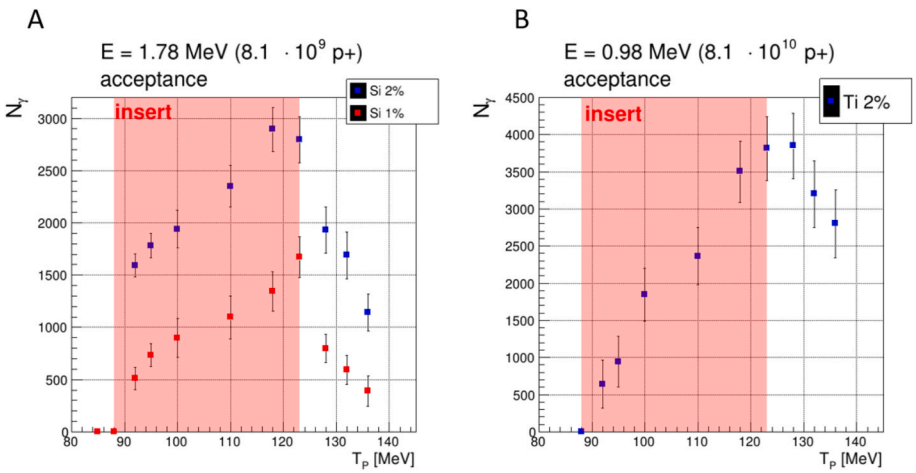

Fig. 8. Simulated tracer signal strength. The assumed detector geometrical acceptance of 0.0027 of full solid angle, 10^8 protons per single spot, 81 spots per a monoenergetic layer. A: signal for silicon, integrated over a single monoenergetic layer, for 1 % tracer concentration (red) and 2% concentration (blue). B: signal for titanium, 2% concentration. In this case, to discriminate signal from background, a ten times larger number of protons must have been simulated. The red areas indicate the beam energy range for which Bragg peaks are completely contained in the tracer-doped insert. (For interpretation of the references to color in this figure legend, the reader is referred to the web version of this article.)

microenvironment inside the tumor tissue, which may sensitize cells to subsequent irradiation with protons or X-rays. This is the result of the generation of reactive oxygen species by metallic nanoparticles [19,56]. The cytotoxicity of NPs depends on their physicochemical properties. The final cytotoxic effect is influenced by the type of metal [57], NPs size, [58], NPs shape [59], as well as synthesis method [60]. Furthermore, this effect may be dependent on the cell lines used [61]. In the case of FeSi NPs, the low toxicity is due to the presence of a silicon shell that masks the harmful iron core – a similar effect was observed for Au NPs covered with a silicon shell [62]. In turn, TiO_2 NPs were evaluated for cytotoxicity against T98G glioma cells – for TiO_2 concentration of 30 μg/ml, survival decreased by only 13 % [63]. In turn, e.g. for lung fibroblast, cytotoxicity decreased by 25 % at a concentration of 0.5 μg /ml [64].

What is important, both types of used NPs differ in shape. As can be seen in Fig. 3, Ti NRs have a longer dimension of about 25 nm and FeSi NPs have a diameter (core + shell) of about 30 nm. The difference in the shape of the NPs can undoubtedly affect the biological properties of the NPs. Under *in vivo* conditions, disk-shaped nanoparticles will preferentially have a greater biodistribution in the lungs and spleen compared to, for example, NPs in the shape of nano-sticks or nano-spheres [65]. The shape also affects the radiosensitizing properties of NPs [66], because the effect of the interaction between protons and NPs depends on the morphology of the NPs (generation of cytotoxic reactive oxygen species, secondary electrons, etc.). The shape of the NPs – in the case of NPs showing surface plasmon resonance (e.g. Au NPs) – affects the position of the peak maximum in the UV–Vis spectrum, which is important in photo-based anticancer therapies [67,68]. Moreover, although the size of both types of NPs appears to be similar, it should be noted that this refers only to a single linear dimension (25 nm for anisotropic Ti NRs vs 30 nm for isotropic spherical FeSi NPs). Shape anisotropy significantly affects various biological properties of NPs—not only their radiosensitizing capabilities (e.g. through differential ROS generation resulting from the interaction of the radiation beam with NPs of varying shapes), but also cellular uptake [69], endocytic pathways [70,71], and intracellular trafficking [72].

The effect of increasing cell survival (or no significant change compared to control cells) under the influence of NPs at low concentrations occurs (although rarely) in biological tests, especially in the relatively poorly sensitive MTS test. In our case, this effect concerned only TiO_2 NPs. A similar effect was observed for human corneal epithelial cells treated with TiO_2 NPs [73], where the survival rate (compared to the control) increased even to a concentration of 100 μg/ml.

Using holotomographic microscopy, it turned out that both TiO_2 NRs and FeSi NPs – based tracers accumulate in cells, although in a different preferred place for glioma cells and normal cells. It is worth emphasizing that our research concerned only cell lines. Cancer and normal cells were cultured separately, and NPs were added to them – it is very possible that the NPs penetrated the normal cells because they had no other choice. Furthermore, these NPs accumulated only on the surface of the cell membrane, and not – as in the case of glioma cells – evenly inside the cells, without a preferential place of accumulation. The situation regarding the uptake of NPs-based tracers may be completely different if we were to use an *in vivo* model. In this case, the tumor consists of interwoven normal and cancerous cells, so it is very possible that the uptake of NPs by glioma cells would be even greater. It would be observable, especially if these NPs were functionalized e.g. using saccharides (e.g. glucose) – glioma cells (but also other cancers) are characterized by increased glucose metabolism and for such biofunctionalized NPs, they would be more willing to penetrate inside the cancer cells, sparing normal cells and tissues.

5.2. *Monte Carlo simulations*

Based on the cross-section diagram in Fig. 1, it can be seen that the signal from titanium should appear earlier in the proximal layers than the silicon signal, as the gamma emission threshold in titanium is lower. In the distal layers, it would be preferred if the signal decreased significantly when the Bragg peak leaves the insert. To ensure this, the PG production cross section for the tracer would need to drop to zero for higher energies, which unfortunately is not the case for any of the investigated tracers. The relative drop is larger for silicon than for titanium. In summary, while a first glance suggests that titanium seems to be better suited for the detection of the proximal tumor surface, silicon is expected to provide better sensitivity at the distal surface.

The results of the simulations performed agree those expectations. In the case of silicon at 2 % mass concentration, its signal was detected in the first monoenergetic layer, for which the Bragg peak was contained in the tumor-mimicking insert – see Fig. 8.

When the Bragg peak moves outside the insert, downstream the distal insert surface, the silicon signal drops significantly.

These results were verified analytically by estimating the expected number of gamma particles on the basis of the cross section from the

TALYS database.

Additional simulations, performed for the silicon mass concentration of 1 % in the insert, exhibit the same correlation. The concentration of 1 % silicon has been proven to be nontoxic for healthy tissues (see *Determination of NPs cytotoxicity – MTS assay*).

Similar results were obtained for the second tracer – titanium. The titanium signal also appeared in the first monoenergetic layer. Its strength, compared to the silicon signal, is much smaller though. However, it should be noted that separating the titanium deexcitation peak from the background is more difficult than for silicon because of the presence of other peaks nearby. The latter affects the precision of signal and background estimation. The signal strength estimated on the basis of the TALYS cross sections was about 13 times higher than that obtained from the simulations. This may indicate that the cross sections included in Geant4 are severely underestimated or the appearance of the neighboring peaks from PMMA in the gamma spectrum hindered a precise fit the 0.98 MeV peak and consequently the estimation of its content. For this reason, further studies using a lower concentration of titanium nanoparticles were not continued.

5.3. Limitations

It should be noted that the results presented in Fig. 8 were obtained for the irradiation of a monoenergetic layer consisting of 81 spots assuming 10^8 protons per spot and 100 % detection efficiency. The phantom emitted isotropically about 4000 gamma quanta per spot, which resulted in the number of registered tracer gamma quanta per single spot of the order of 10 in the investigated scenario of gamma detection, where the assumed acceptance of the detector was 0.0027 of full solid angle. This is by far insufficient to form a statistically significant signal, thus a summation over a monoenergetic layer was necessary. The assumption about the spot strength is fulfilled for the distal spots, while the proximal ones are typically irradiated with up to ten times less protons [45]. This modifies the statistical significance of the registered signal, and so does the fact that the detection efficiency of a detector similar to the simulated one is of about 11 % for the silicon signal and 19 % for the titanium signal [35]. Taking all these factors into account is necessary when designing the detection setup for the method, since the use of more than one such detector may turn out necessary. Another potential issue is the count-rate capability of the detectors. The expected count rate in the presented scenario is of the order of 1 Mcps, which calls for use of segmented rather than monolithic germanium detectors. Alternatively, one can consider also modern inorganic scintillators with high count-rate capability. Although they cannot compete with germanium detectors as regards the energy resolution, they have been found sufficient to detect silicon signal e.g. in [9]. Presented studies constitute the first step to extended analysis, that will include experimental verification of the simulation results.

In the biological part of the study, some aspects were not investigated, such as whether the nanoparticles are available in the intended mode of injection and their stability in environments more complex than cell culture. These aspects will be further explored in future studies conducted within the research group. A more in-depth investigation into the influence of individual reaction parameters (such as type of precursors, stabilizer, temperature etc.) on the morphology of the obtained NPs, as well as on the synthesis yield, was not conducted, because it was not the main objective of this study.

6. Conclusions

This work contributes to the feasibility study of an online method for determining the Bragg peak position in proton therapy based on beam-activated tracers and their PG radiation. We have focused on two tracer elements, silicon and titanium, applied in the form of nanoparticles. We have demonstrated that both types of nanoparticles can be successfully used in dual mode as radiosensitizers, as well as for effective monitoring of the course of tumor irradiation with a proton beam.

Biologically, both investigated small NP types turned out to have similar properties: they have similar cytotoxicity to cells and radiosensitizing properties, which are particularly visible towards cancer cells irradiated with a high-energy proton beam. However, the selected concentration of NPs, as well as the radiation dose by themselves do not cause a significant cytotoxic effect. In terms of physical properties, some differences were observed. Titanium turned out to be suboptimal for applications in proton therapy due to insufficient signal drop in the distal layers of the test, which does not allow one to determine the position of the Bragg peak in that region. The potential use of titanium in proton therapy would have to be limited to those solutions in which instead of selectively delivering nanoparticles to tumor, a material containing the appropriate amount of titanium could be placed between the sensitive structure and the tumor. However, this would involve unwanted delivery of the dose to the OAR and the procedure described above would only partially mitigate the harmful effects. Silicon, on the other hand, seems to have optimal biological and physical properties to be used in determining whether or not the Bragg peak is contained in the tumor volume. However, its physical properties should be tested under experimental conditions close to clinical ones. This requires the appropriate selection of the detection system. In this case, a good solution seems to be the use of segmented semiconductor detectors with a sufficiently fast data acquisition system to be able to register prompt-gamma radiation. The method implementation would also greatly benefit from enlarging the acceptance of the whole detection system. Subsequently, the research described in this article should be extended to studies in animals, which provide insight into NPs delivery chain and metabolism.

Funding

This work was supported by the Priority Research Area Digiworld under the program Excellence Initiative – Research University at the Jagiellonian Universit in Kraków, and additionally by the Polish National Science Centre (grant 2017/26/E/ST2/00618). The collaboration between Polish and German partners was possible thanks to the support of the Polish National Agency for Academic Exchange as well as the German Academic Exchange Service (project ID 57562042).

Declaration of competing interest

The authors declare that they have no known competing financial interests or personal relationships that could have appeared to influence the work reported in this paper.

Acknowledgements

Hearty thanks to the employees of the Bronowice Cyclotron Centre for their substantive support and assistance in conducting experiments.

Appendix A. Supplementary data

Supplementary data to this article can be found online at https://doi.org/10.1016/j.ejmp.2025.105068.

References

[1] Wrońska A, Dauvergne D. Range verification by means of prompt-gamma detection in particle therapy. In: Iniewski K, Iwańczyk J, editors. Radiation Detection Systems, Vol 2. CRC Press/Routledge; 2021. p. 139–60.
[2] Paganetti H, Botas P, Sharp GC, Winey B. Adaptive proton therapy. Phys Med Biol. 2021 Nov 15;66:22.
[3] Paganetti H. Range uncertainties in proton therapy and the role of Monte Carlo simulations. Phys Med Biol. 2012;57:R99–.
[4] Taasti VT, Hattu D, Vaassen F, et al. Treatment planning and 4D robust evaluation strategy for proton therapy of lung tumors with large motion amplitude. Med Phys. 2021;48:4425–37.

[5] Zhang J, Xu XG, Shi C, et al. Development of a geometry-based respiratory motion–simulating patient model for radiation treatment dosimetry. J Appl Clin Med Phys. 2008;9:16–28.
[6] Penninckx S, Hespeels F, Smeets J, et al. Metallic Nanoparticles: A Useful Prompt Gamma Emitter for Range Monitoring in Proton Therapy? Radiation. 2021;1:305–16.
[7] Ibáñez-Moragues M, Fernández-Barahona I, Santacruz R, et al. Zinc-Doped Iron Oxide Nanoparticles as a Proton-Activatable Agent for Dose Range Verification in Proton Therapy. Molecules. 2023;28.
[8] Cartechini G, Fogazzi E, Hart S-D, et al. Loading the tumor with 31P, 63Cu and 89Y provides an in vivo prompt gamma-based range verification for therapeutic protons. Front Phys. 2023;11.
[9] Galanakou P, Leventouri T, Muhammad W. Non-radioactive elements for prompt gamma enhancement in proton therapy. Radiation Physics and Chemistry. 2022;196:110132.
[10] Martins PM, Freitas H, Tessonnier T, et al. Towards real-time PGS range monitoring in proton therapy of prostate cancer. Sci Rep. 2021;11.
[11] Joudeh N, Linke D. Nanoparticle classification, physicochemical properties, characterization, and applications: a comprehensive review for biologists. J Nanobiotechnology. 2022;20:1–29.
[12] Klębowski B, Depciuch J, Parlińska-Wojtan M, et al. Applications of Noble Metal-Based Nanoparticles in Medicine. Int J Mol Sci. 2018;19.
[13] Bromma K, Cicon L, Beckham W, et al. Gold nanoparticle mediated radiation response among key cell components of the tumour microenvironment for the advancement of cancer nanotechnology. Sci Rep. 2020;10.
[14] Salado-Leza D, Traore A, Porcel E, et al. Radio-Enhancing Properties of Bimetallic Au:Pt Nanoparticles: Experimental and Theoretical Evidence. Int J Mol Sci. 2019;20.
[15] Zhao J, Liu P, Ma J, et al. Enhancement of Radiosensitization by Silver Nanoparticles Functionalized with Polyethylene Glycol and Aptamer As1411 for Glioma Irradiation Therapy. Int J Nanomedicine. 2019;14:9483–96.
[16] Meyer TJ, Scherzad A, Moratin H, et al. The Radiosensitizing Effect of Zinc Oxide Nanoparticles in Sub-Cytotoxic Dosing Is Associated with Oxidative Stress In Vitro. Materials. 2019;12:4062.
[17] Sisin NNT, Razak KA, Abidin SZ, et al. Radiosensitization Effects by Bismuth Oxide Nanoparticles in Combination with Cisplatin for High Dose Rate Brachytherapy. Int J Nanomedicine. 2019;14:9941–54.
[18] Maggiorella L, Barouch G, Devaux C, et al. Nanoscale radiotherapy with hafnium oxide nanoparticles. Future Oncology. 2012;8:1167–81.
[19] Morita K, Nishimura Y, Nakamura S, et al. Titanium oxide nano-radiosensitizers for hydrogen peroxide delivery into cancer cells. Colloids Surf B Biointerfaces. 2021;198.
[20] Chen S, Han F, Huang D, et al. Fe_3O_4 magnetic nanoparticle-enhanced radiotherapy for lung adenocarcinoma via delivery of siBIRC5 and AS-ODN. J Transl Med. 2021;19:1–14.
[21] Sanchez GJ, Maury P, Stefancikova L, et al. Fluorescent radiosensitizing gold nanoparticles. Int. J. Mol. Sci. 2019;20:4618.
[22] Le Duc G, Miladi I, Alric C, et al. Toward an image-guided microbeam radiation therapy using gadolinium-based nanoparticles. ACS Nano 2011;5:9566–74.
[23] Chargari C, Maury P, Texier M, et al. Theragnostic gadolinium-based nanoparticles safely augment X-ray radiation effects in patients with cervical cancer. ACS Nano 2024;18:16516–29.
[24] Porcel E, Liehn S, Remita H, et al. Platinum nanoparticles: a promising material for future cancer therapy? Nanotechnology 2010;21:85103.
[25] Li S, Porcel E, Remita H, et al. Platinum nanoparticles: an exquisite tool to overcome radioresistance. Cancer Nanotechnol. 2017;8:4.
[26] Schuemann J, Bagley AF, Berbeco R, et al. Roadmap for metal nanoparticles in radiation therapy: current status, translational challenges, and future directions. Phys Med Biol. 2020;65:21RM02.
[27] Dayem AA, Hossain MK, Bin LS, et al. The Role of Reactive Oxygen Species (ROS) in the Biological Activities of Metallic Nanoparticles. Int J Mol Sci. 2017;18.
[28] Paciorek P, Zuberek M, Grzelak A. Products of Lipid Peroxidation as a Factor in the Toxic Effect of Silver Nanoparticles. Materials. 2020;13.
[29] Zainudin NHM, Sisin NNT, Rashid RA, et al. Cellular analysis on the radiation induced bystander effects due to bismuth oxide nanoparticles with 6 MV photon beam radiotherapy. J Radiat Res Appl Sci. 2022;15:318–25.
[30] Hoshyar N, Gray S, Han., H., Bao., G. The effect of nanoparticle size on in vivo pharmacokinetics and cellular interaction. Nanomedicine (London) 2016;11:673–92.
[31] Zuckerman JE, Choi CHJ, Han H, Davis ME. Polycation-siRNA nanoparticles can disassemble at the kidney glomerular basement membrane. Proc. Natl. Acad. Sci. U S A 2012;109:3137–42.
[32] Rosero WAA, Barbezan AB, de Souza CD, Rostelato MECM. Review of advances in coating and functionalization of gold nanoparticles: from theory to biomedical application. Pharmaceutics 2024;16:255.
[33] Su S, Kang PM. Systematic review of biodegradable nanomaterials in nanomedicine. Nanomaterials (Basel) 2020;10:656.
[34] TALYS - Nuclear reaction model code;https://nds.iaea.org/talys/.
[35] SRIM - The Stopping and Range of Ions in Matter; http://srim.org/.
[36] Kelleter L, Wrońska A, Besuglow J, et al. Spectroscopic study of prompt-gamma emission for range verification in proton therapy. Physica Medica. 2017;34:7–17.
[37] Brunette DM, Tengvall P, Textor M, et al. Titanium in Medicine. Berlin, Heidelberg: Springer; 2001.
[38] Zhang Z, Zhong X, Liu S, et al. Aminolysis route to monodisperse titania nanorods with tunable aspect ratio. Angew Chem Int Ed Engl. 2005;44:3466–70.
[39] Maximenko A, Depciuch J, Łopuszyńska N, et al. Fe3O4@SiO2@Au nanoparticles for MRI-guided chemo/NIR photothermal therapy of cancer cells. RSC Adv. 2020;10:26508–20.
[40] Wee CW. Radiotherapy for Newly Diagnosed Glioblastoma in the Elderly: What Is the Standard? Brain Tumor Res Treat. 2022;10:12.
[41] Buch K, Peters T, Nawroth T, et al. Determination of cell survival after irradiation via clonogenic assay versus multiple MTT Assay - A comparative study. Radiation Oncology. 2012;7:1–6.
[42] Geant4 - Toolkit for the simulation of the passage of particles through matter; https://geant4.web.cern.ch/.
[43] Akagi T, Aso T, Iwai G, et al. Geant4-based particle therapy simulation framework for verification of dose distributions in proton therapy facilities. Progress in Nuclear Science and Technology. 2014;4:896–900.
[44] Wrońska A, Kasper J, Ahmed AA, et al. Prompt-gamma emission in GEANT4 revisited and confronted with experiment. Physica Medica. 2021;88:250–61.
[45] Welcome to the Guide for Physics Lists!; https://geant4-userdoc.web.cern.ch/UsersGuides/PhysicsListGuide/BackupVersions/V10.4/html/index.html.
[46] Krimmer J, Dauvergne D, Létang JM, É.. Testa Prompt-gamma monitoring in hadrontherapy: a review. Nucl Instrum Methods A. 2018;878:58–73.
[47] Pausch G, Berthold J, Enghardt W, et al. Detection systems for range monitoring in proton therapy: Needs and challenges. Nucl Instrum Methods Phys Res A. 2020;954.
[48] Verburg JM, Seco J. Proton range verification through prompt gamma-ray spectroscopy. Phys Med Biol. 2014;59:7089–106.
[49] Gajewski J, Garbacz M, Chang C-W, et al. Commissioning of GPU–Accelerated Monte Carlo Code FRED for Clinical Applications in Proton Therapy. Front Phys. 2021;8.
[50] Antcheva I, Ballintijn M, Bellenot B, et al. ROOT - A C++ Framework for Petabyte Data Storage, Statistical Analysis and Visualization. Comput Phys Commun. 2011;180:2499–512.
[51] Klębowski B, Stec M, Depciuch J, et al. Improving the Effect of Cancer Cells Irradiation with X-rays and High-Energy Protons Using Bimetallic Palladium-Platinum Nanoparticles with Various Nanostructures. Cancers (Basel). 2022;14.
[52] Klębowski B, Depciuch J, Stec M, et al. Fancy-Shaped Gold–Platinum Nanocauliflowers for Improved Proton Irradiation Effect on Colon Cancer Cells. Int J Mol Sci. 2020;21:9610.
[53] Bendale Y, Bendale V, Paul S. Evaluation of cytotoxic activity of platinum nanoparticles against normal and cancer cells and its anticancer potential through induction of apoptosis. Integr Med Res. 2017;6:141–8.
[54] Repotente EC, Carreon AJ, Devanadera MK, et al. Cytotoxic potential on human breast and lung cancer cells of the biosynthesized gold nanoparticles from the reduction of chloroauric acid by lactic acid isolated from Lactobacillus acidophilus. Front Mater. 2022;9:600.
[55] Arab-Bafrani Z, Shahbazi-Gahrouei D, Abbasian M, et al. Multiple MTS Assay as the Alternative Method to Determine Survival Fraction of the Irradiated HT-29 Colon Cancer Cells. J Med Signals Sens. 2016;6:112.
[56] Zhang J, Shi J, Han S, et al. Titanium dioxide nanoparticles induced reactive oxygen species (ROS) related changes of metabolomics signatures in human normal bronchial epithelial (BEAS -2B) cells. Toxicol Appl Pharmacol. 2022;444:116020.
[57] Shkryl Y, Rusapetova T, Yugay Y, Egorova A, Silant'ev, V., Grigorchuk, V., Karabtsov, A., Timofeeva, Y., Vasyutkina, E., Kudinova, O, et al. Biosynthesis and Cytotoxic Properties of Ag, Au, and Bimetallic Nanoparticles Synthesized Using Lithospermum erythrorhizon Callus Culture Extract. Int. J. Mol. Sci. 2021;22:9305.
[58] Park MV, Neigh AM, Vermeulen JP, et al. The effect of particle size on the cytotoxicity, inflammation, developmental toxicity and genotoxicity of silver nanoparticles. Biomaterials. 2011;32(36):9810–7. https://doi.org/10.1016/j.biomaterials.2011.08.085.
[59] Steckiewicz KP, Barcinska E, Malankowska A, et al. Impact of gold nanoparticles shape on their cytotoxicity against human osteoblast and osteosarcoma in in vitro model. Evaluation of the safety of use and anti-cancer potential. J Mater Sci Mater Med. 2019;30(2):22.
[60] Depciuch J, Stec M, Maximenko A, et al. Synthesis method-dependent photothermal effects of colloidal solutions of platinum nanoparticles used in photothermal anticancer therapy. Appl Organometal Chem. 2020;34:e5401.
[61] Shawki MM, El Sadieque A, Elabd S, Moustafa ME. Synergetic Effect of Tumor Treating Fields and Zinc Oxide Nanoparticles on Cell Apoptosis and Genotoxicity of Three Different Human Cancer Cell Lines. Molecules 2022,;27;4384..
[62] Kim MJ, Jung DH, Lee CY, Hong S, Heo JH, Lee JH. Structurally Engineered Silica Shells on Gold Nanorods for Biomedical Applications. Small Struct. 2023;4:2300047.
[63] Fuster E, Candela H, Estévez J, Vilanova E, Sogorb MA. Titanium Dioxide, but Not Zinc Oxide, Nanoparticles Cause Severe Transcriptomic Alterations in T98G Human Glioblastoma Cells. Int. J. Mol. Sci. 2021;22:2084.
[64] Patil NA, Gade WN, Deobagkar DD. Epigenetic modulation upon exposure of lung fibroblasts to TiO2 and ZnO nanoparticles: alterations in DNA methylation. Int J Nanomedicine. 2016;11:4509–19.
[65] Blanco E, Shen H, Ferrari M. Principles of nanoparticle design for overcoming biological barriers to drug delivery. Nat Biotechnol 2015;33:941–51.
[66] Ma N, Wu FG, Zhang X, et al. Shape-Dependent Radiosensitization Effect of Gold Nanostructures in Cancer Radiotherapy: Comparison of Gold Nanoparticles, Nanospikes, and Nanorods. ACS Appl Mater Interfaces. 2017;9(15):13037–48.
[67] Pakravan A, Salehi R, Mahkam M. Comparison study on the effect of gold nanoparticles shape in the forms of star, hallow, cage, rods, and Si-Au and Fe-Au

core-shell on photothermal cancer treatment. Photodiagnosis Photodyn Ther. 2021;33:102144.
[68] Adnan NNM, Cheng YY, Ong NMN, Kamaruddin TT, Rozlan E, Schmidt TW, et al. Effect of gold nanoparticle shapes for phototherapy and drug delivery. Polym Chem. 2016;7(16):2888–903.
[69] Potrc T, Kralj S, Nemec S, Kocbek P, Kreft ME. The shape anisotropy of magnetic nanoparticles: an approach to cell-type selective and enhanced internatlization. Nanoscale 2023;15:8611–8.
[70] Li, Y., Yue, T., Yang, K., Zhang, X. Molecular modeling of the relationship between nanoparticle shape anisostropy and endocytosis kinetics. Biomaterials 2012;33: 4965-4973.
[71] Xie X, Liao J, Shao X, Li Q, Lin Y. The effect of shape on cellular uptake of gold nanoparticles in the forms of stars, rods, and triangles. Sci. Rep. 2017;7:3827.
[72] Diloknawarit B, Lee K, Choo P, Odom TW. Nanoparticle anisotropy increases targeting interactions on live-cell membranes. ACS Nano. 2024;18:12537–46.
[73] Li X, Kang B, Eom Y, et al. Comparison of cytotoxicity effects induced by four different types of nanoparticles in human corneal and conjunctival epithelial cells. Sci Rep 2022;12:155.